Journal of Fluids and Structures 121 (2023) 103947

Contents lists available at ScienceDirect

Journal of Fluids and Structures

journal homepage: www.elsevier.com/locate/jfs

Influence of travelling waves on the fluid dynamics of a beam submerged in water

Skriptyan N.H. Syuhri [a,b,*], David Pickles [a], Hossein Zare-Behtash [a], Andrea Cammarano [a]

[a] James Watt School of Engineering, University of Glasgow, UK
[b] Department of Mechanical Engineering, University of Jember, Indonesia

ARTICLE INFO

Article history:
Received 21 January 2023
Received in revised form 23 May 2023
Accepted 24 June 2023
Available online 12 July 2023

Keywords:
Travelling waves
Beam structure
Vibration pattern
Fluid flow
Fluid–structure interaction
Laser Doppler anemometry

ABSTRACT

Inspired by the use of travelling waves for propulsion mechanisms adopted by many animals and organisms, this paper investigates the mechanism with which travelling waves in beam-like structures induce velocity in a surrounding fluid. This work focuses on the flow induced around the beam tip and provides an experimental characterisation of the phenomena. A test rig equipped with Laser Doppler Anemometry (LDA) is used to investigate the induced fluid velocity and its dependency on the modal response of the beam. Numerical simulations are performed to complement the experimental tests and provide further insight into the fluid–structure interaction. The numerical model also allows for the beam vibration envelope and vibration patterns to be obtained and correlated with the measured fluid velocity. Several geometrical variations are considered in the analysis over a range of frequencies that encompass resonant responses up to the fourth mode. The results showed that the fluid flow is only marginally affected by the change in the vibration pattern between the first-two resonant mode; the induced fluid velocity and, hence, the thrust are mostly driven by the tip velocity of the beam.

1. Introduction

Travelling waves in vibrating structures submerged in liquid have been utilised in many engineering applications. It has been demonstrated that submerged beams can be utilised for transport (Malladi, 2016) or pumping devices (Nisar et al., 2008; Wang and Fu, 2018). If the beam is clamped at each end, it creates a force that pushes the surrounding liquid in the axial direction. This configuration was used by Ogawa et al. (2009) to drive a liquid pumping device by utilising nine piezoelectric patches distributed evenly along the length of the beam. The pumping action was achieved by applying sinusoidal voltages with a phase difference of 120° between each piezoelectric. Following this investigation, the performance of actuation mechanisms for pumping devices was further improved in Ye et al. (2014) and Yu et al. (2015), where magnetic-based actuators were used to substitute the piezoelectric patches. The magnetic actuation was achieved by mounting four cylindrical magnets on the beam surface that are separated equally along the beam length. Furthermore, the poles are arranged in a way that it creates a 90-degree phase delay between each pole. Although the use of four magnets on the beam surface can limit miniaturisation, this actuation solution generated more force than the piezoelectric counterpart, hence, resulting in a higher flow rate (Ye et al., 2014; Yu et al., 2015; Liu and Zhang, 2017).

---

* Correspondence to: James Watt South Building, University of Glasgow, Glasgow, G12 8QQ, United Kingdom.
E-mail address: s.syuhri.1@research.gla.ac.uk (S.N.H. Syuhri).

https://doi.org/10.1016/j.jfluidstructs.2023.103947

In the case of free-free boundary conditions, the beam vibration and interaction with the surrounding fluid can generate thrust for self-propelling devices (e.g., artificial swimmers and robotic fish). The literature presents studies of the relationship between vibration characteristics and the forward velocity induced on the surrounding fluid and highlights that different structural mode shapes interact with the surrounding media in different ways. The first two mode shapes of a cantilever beam, for example, resemble thunniform fish locomotion. Parametric studies have been conducted to address the influence of beam geometries on the propulsive performance of the beam around these low mode shapes (Erturk and Delporte, 2011; Shahab et al., 2015). Shahab et al. (2015), for instance, demonstrated that the mean thrust for this configuration is proportional to the beam width and length. Erturk and Delporte (2011) increased the thrust through the addition of a caudal fin at the free end of the cantilever beam. The fluid dynamics of the beam tip have been thoroughly investigated in Demirer (2021), Fernández-Prats et al. (2015), Piñeirua et al. (2017), Shelton et al. (2014), Yeh (2016), allowing the role of other important parameters such as flexural stiffness, tailbeat frequency, heaving and pitching mode, and phase lag on the generation of thrust to be highlighted. Recently, further improvements have been attempted through the use of smart materials and nature inspired geometries (Erturk and Delporte, 2011; Cen and Erturk, 2013; Shahab and Erturk, 2015, 2016), however the sensitivity of thrust to small changes in frequency, especially close to resonance, remains a considerable limitation.

In higher mode shapes, the cantilever beam can mimic anguilliform locomotion such as eels and lamprey (Cui et al., 2018) and therefore are considered more promising for propulsive applications, as concluded by the numerical and experimental studies in Piñeirua et al. (2017), Dryden and Ballard (2021), Godoy-Diana and Thiria (2018), Piñeirua et al. (2015), Ramananarivo et al. (2014a,b), Raspa et al. (2014). Ramananarivo et al. (2013), though, reported that the forward velocity in this configuration depends on the beam tip velocity: a shorter beam can generate higher velocities compared to a longer beam. This is due to the energy dissipation caused by the surrounding fluid, which results in reduced vibration amplitudes. This phenomenon also creates a phase delay between the displacements at the free ends of the beam, which is conducive to travelling waves. This is also known as progressive waves or propagating waves in the vibration pattern (Ramananarivo et al., 2014a).

Since the dissipation energy in the beam depends on many parameters – boundary conditions, forcing frequencies and amplitudes, to name a few – the nature of the vibrational wave in the beam can be easily affected, going from pure standing to pure travelling waves. Commonly a mixture of travelling and standing waves is observed (Malladi, 2016), with amplification of standing waves mostly occurring at resonance for particular beam configurations. Nonetheless, researchers have developed techniques to amplify the amplitude of travelling waves whilst reducing the amplitude of standing waves over a wide range of frequencies. Using magnetic induction, for instance, a combination of permanent and electro-magnets can be used to induce a distribution of repulsive and attractive forces on the beam. Using a force distribution with two or more forces 90 degrees out of phase and at the same amplitude, high-amplitude travelling waves can be generated over a wide range of frequencies, as demonstrated by Ye et al. (2014). Although very promising, the implementation of this method presents some challenges due to the precision required to control the force distribution. An alternative actuation method using piezoelectric patches mounted on the beam surface at different positions is presented by Musgrave (2021). This would allow the phase and amplitude of the free tips to be controlled more precisely. However, the work from Malladi et al. (2017) shows that, by varying the phase difference of the two piezoelectric actuators to excite the third mode, a discrepancy exists between the predicted and generated thrust induced by the travelling waves.

A comprehensive study that relates the characteristics of the travelling wave to the thrust it induces is lacking. Since diverse and sometimes contradicting results are found in the literature, a more systematic approach to monitor the fluid–structure interaction is here proposed. In this paper an experimental rig that allows for the quantification of the thrust produced by the travelling wave is presented. The results are used to assess the influence of several geometrical parameters including the thickness of the beam. In addition, this work extends previous studies by considering travelling waves in frequency ranges up to the fourth resonant frequency, as well as the measurement of the influence on the (forward) velocity induced in the fluid. This will provide further insight into the complex interaction between travelling waves in structures and the surrounding media and will be conducive to enhance thrust generation using travelling waves.

2. Experimental investigation

The schematic diagram of the experimental setup for the fluid measurements is illustrated in Fig. 1. Fig. 1(a) depicts the test rig configuration which consists of a metal beam submerged in a 40 *x* 25 *x* 25 cm tank filled with 23.5 L of water. The submerged beam was attached to an LDS V201 electrodynamic shaker using an L-shaped extension plate. This configuration results in a base excited cantilevered beam (the constrain of the cantilever undergoes a prescribed motion). The extension plate was made of stainless-steel materials with a thickness of about 10 times that of the beam, resulting in its first natural frequency being higher than the operating frequencies of the beam to avoid interference. A PCB Piezotronics Model 352C22 accelerometer was mounted at each end of the extension plate. The accelerometer, located at the clamped section of the beam, was used to monitor that the desired base excitation was achieved, while a second accelerometer on the shaker base was used to ensure that the extension plate movement could be approximated as a rigid body. The two accelerometers were amplified by a PCB Piezotronics Model 428C signal amplifier, before being connected to a DAQ. A PicoScope 2405A USB Oscilloscope was used to acquire the signal as well as generate the input signal for the shaker. The output of the signal generator was amplified by a 48 W LDS PA25E power amplifier.

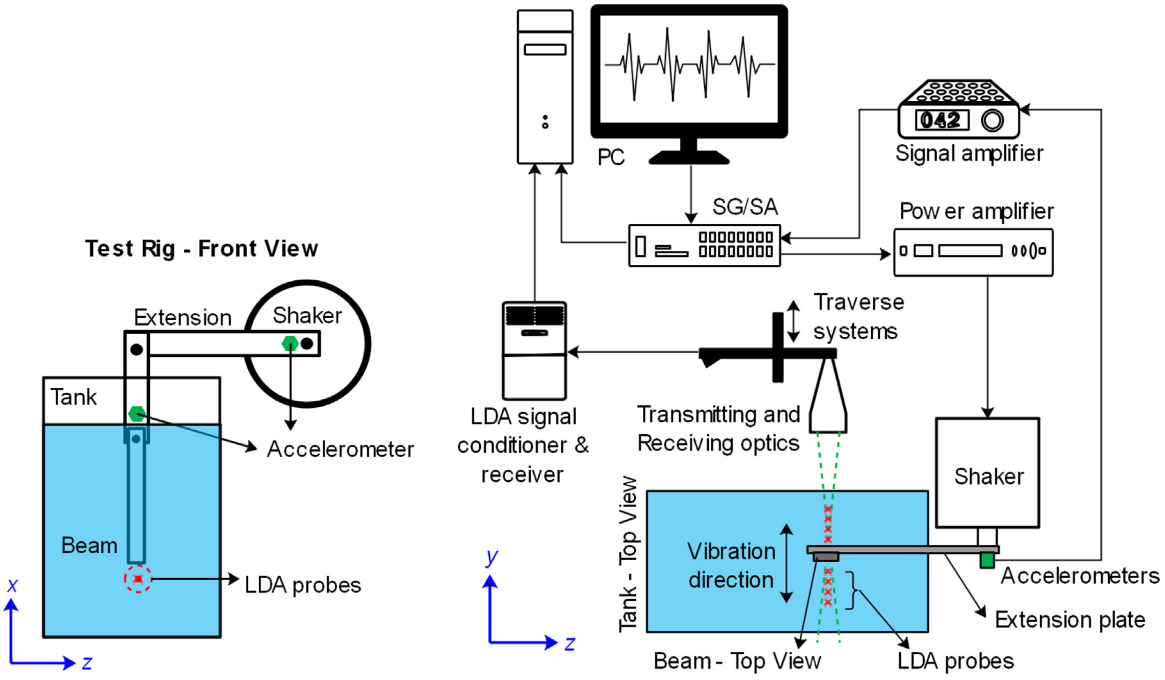

(a) (b)

Fig. 1. (a) The front view of the test rig, and (b) The schematic diagram of the experimental test with the beam, tank and extension plate shown in the top view.

A commercially available Dantec Dynamics two component Laser Doppler Anemometry system was used to measure the velocity profile produced by the moving beam 5 mm below the tip of the beam ($x = 0.140$ m) on a plane in-line with the centre of the beam. The location of the sampled points is indicated by the red cross in Fig. 1(a). Fig. 1(b) shows the schematic of the acquisition/excitation chain used in the experiments. The system comprises of two lasers, a Bragg cell, transmitting and receiving optics, and a traverse system. Two diode-pumped solid-state 1 W lasers with wavelengths of 488 nm and 514 nm were used to generate continuous laser beams. The measurement probe consists of (laser) beam splitters, a focusing lens and receiving optics. The lasers were oriented at an angle of 2.5° to create a measurement volume of $2.62 \times 0.12\ x\ 0.12$ mm^3. Silver-coated hollow glass spheres, with a mean particle diameter of 10 µm, were used to homogenously seed the water tank. The seeding particles reflect the fringe pattern generated by the laser beams back into the head of the probe. Analysis of the frequency shift of the scattered fringe pattern allows the velocity of the particle passing through the measurement volume to be calculated (Zhang, 2010). The measurement probe was mounted on a Dantec 9041T3332 2D traverse system resulting in a spatial resolution of ± 0.01 mm.

Fig. 2 displays the xy-plane through the axis of the beam and the velocity measurement locations. The beam – black rectangle in Fig. 2 – had a length of 0.135 m and vibrated in the yz-plane. The beam length remains constant throughout the study, whilst different beam thicknesses are examined. In an ideal case, the beam oscillation in the y-direction induces movement of the surrounding liquid in the xy-plane (no out-of-plane movement). Since the LDA system monitors the fluid velocity in the x- and z-directions, this setup allows for the measurement of the x-velocity component (horizontal) only. Although the 2D traverse system is capable of moving across the xy-plane, the measurement location was maintained at 5 mm downstream from the tip of the beam ($x = 0.140$ m). This is to prevent the LDA lasers to hit the beam and its reflections to damage the receiving optics. The traverse system was operated to measure velocities in the y-axis from -0.025 m to 0.025 m. Schematics of the velocity measurements and direction of the fluid in the xy-plane is illustrated with red arrows in Fig. 2.

The oscillating beam used in the test has dimensions of 135 mm x 12.75 mm x 0.6 mm. The density of the beam is approximately 8442 kg/m^3. The flexural rigidity, EI, of the cantilever beam has been estimated by correlating the geometry and the density to the natural frequencies of the beam as follows (Inman, 2013):

$$EI = \frac{\omega_n^2 \rho A}{\beta_n^4} \qquad (1)$$

where, E is the modulus of elasticity, ρ is the density of the material, A is the cross-sectional area, I is the second moment of area, ω_n and β_n are the natural frequency and the wave number at the nth mode, respectively. The first-four values of $\beta_n L$ for the cantilever beam configuration are 1.8751, 4.6941, 7.8548 and 10.9955.

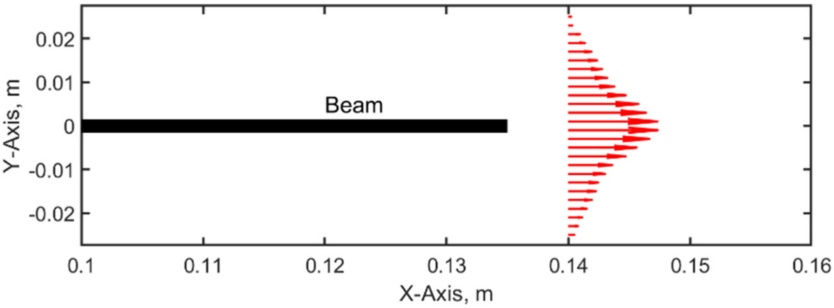

Fig. 2. Fluid measurement location relative to the beam.

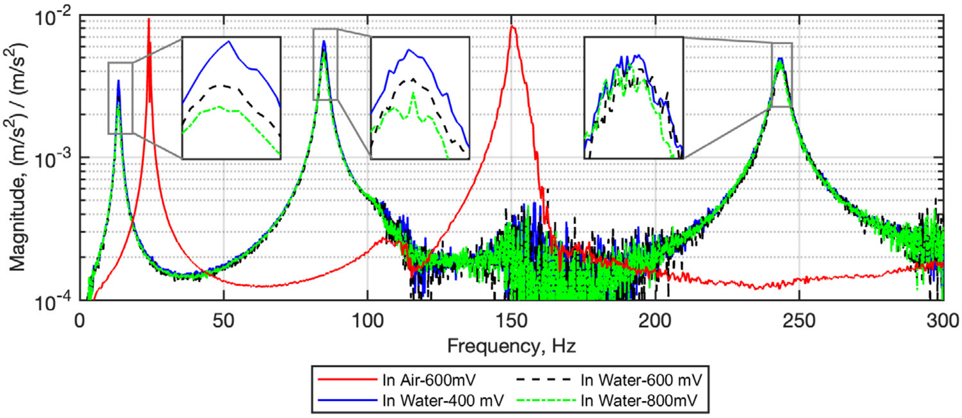

Fig. 3. The FRF of the beam with the thickness of 0.6 mm obtained from experiments.

The natural frequencies can be extracted from the peaks of the beam transmissibility frequency response function (FRF). A Data-Physics Quattro spectrum analyser was used to measure the FRF of the beam: this was computed considering the transfer function between the velocity at the free tip of the beam, measured by a Polytec PDV-100 laser vibrometer, and the acceleration at the base, measured with the PCB accelerometer, mounted on the clamped section of the beam. More information on the structural characterisation of the beam can be found in Syuhri et al. (2022). Fig. 3 presents the FRFs of the 0.6 mm beam from the experimental measurements in two different media: air and water. The beam was subjected to a random excitation with a frequency content in the range 0–600 Hz. Note that the magnitude of the FRF is the ratio between the tip and the base acceleration. Since the laser vibrometer measures velocities, the signal analyser automatically converts these into accelerations to obtain a dimensionless ratio. This process which might include filtering procedures can affect the amplitude of the acceleration responses. Therefore, the FRF magnitude in Fig. 3 may be underestimated. However, the location of the peaks, i.e., their frequency, is not affected.

In Fig. 3, the red line demonstrates the FRF of the beam vibrating in the air with a maximum random amplitude of 600 mV. Note that the gain for the power amplifier was set constant to 3 for all FRF measurements. Therefore, the maximum amplitude after amplification was about 4.6 V. The characteristics of the output voltage of the power amplifier with respect to different gain levels are described in our previous paper in Syuhri et al. (2020a). Because the system in air behaves linearly, the beam FRF is independent of the base amplitude: this was assessed by repeating the experiment at different base amplitudes (the FRFs obtained are identical and therefore are not shown here for brevity). This is an indication that the aerodynamic forces are negligible with respect to the elastic forces. This also suggests that the linear characteristic observed for the damping forces is predominantly caused by material damping, as shown in Wagg and Neild (2015), using the Galerkin approach in conjunction with the Euler–Bernoulli beam equation. For the beam vibrating underwater, the maximum amplitudes of the random signals were varied at 400 mV, 600 mV and 800 mV represented in Fig. 3 with the blue, black, and green lines, respectively. Unlike in air, it is observed that the FRF magnitude of the responses in water decreases with increasing input amplitudes. This change in FRF, particularly for large displacements, is due to nonlinear fluid forces: these can be approximated with a quadratic function (Syuhri et al., 2020b). For small displacements, the quadratic part of the damping function becomes negligible and the damping forces can be assumed to be linear. Consequently, the FRF for the small displacement become independent from the input amplitudes. In addition, it is worth mentioning that, while random input signals can offer quick estimation of the modal properties of the beam, periodic input signals such as the stepped-sine wave with controlled base amplitudes are more appropriate for assessing the beam.

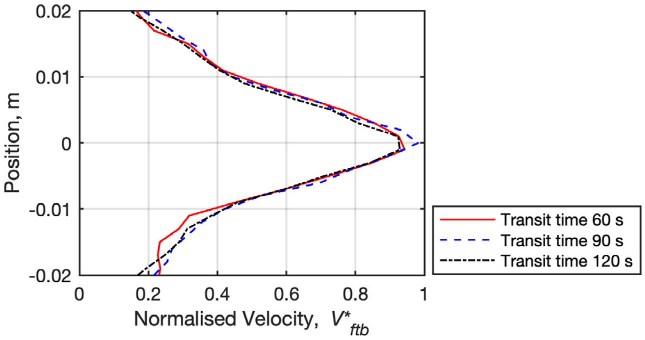

Fig. 4. LDA velocity profiles were generated at the forcing frequency of 18 Hz and the base amplitude of 1.8 mm. The normalised velocity, V^*_{ftb}, is the ratio of the induced mean fluid velocity to the maximum base velocity of the beam.

The first three peaks of the FRF in air occur at frequencies of approximately 24 Hz, 150 Hz and 424 Hz. Substituting these natural frequencies into Eq. (1), a mean flexural rigidity, EI, of approximately 0.0397 N m^2 with a variance of approximately 4.6% has been estimated. Note that discrepancies in the flexural rigidity for different natural frequency values may be caused by nonlinearities in the beam, affecting the term E, I or a combination of the two. Fig. 3 shows that, when the beam vibrates underwater, the FRF magnitude of the first resonant peak is lower than the magnitude of the second and third peaks. The first three natural frequencies from the measurement of the beam submerged in water are approximately 13.48 Hz, 84.77 Hz and 243 Hz. It is noticed that the presence of water results in a drop of the beam's natural frequencies of about 56%. Therefore, the liquid affects not only to the damping force but also the linear mass per unit length. By considering the fluid effect, the relationship between the flexural rigidity and natural frequencies can be expressed by

$$EI_w = \left(\frac{\rho A + \pi \rho_w b^2/4}{\beta_n^4}\right)\omega_{n,w}^2 \tag{2}$$

where b is the beam width; the subscript w stands for water (Ramananarivo et al., 2014a). Using Eq. (2), the equivalent mean flexural rigidity is approximately 0.0379 N m^2 with a variance of approximately 4.6%.

The traverse system was set to scan 5 cm along the y-axis with an increment of 2 mm, creating a total of 26 measurement points. To generate an average flow velocity contour along the y-axis, the LDA system was operated in burst mode with a constant sampling time for every measurement station. To examine the dependency of the mean fluid velocity on the sample time – the acquisition time at each location – the beam was arbitrarily actuated with a forcing frequency and base amplitude of 18 Hz and 1.8 mm, respectively. The sampling time was varied from 60 s to 120 s with steps of 30 s and the results are presented in Fig. 4. Note that it took approximately 52 min to complete the velocity measurements with a transit time of 120 s. It is evident from the figure that the transit time did not have a significant impact on the results. Nonetheless, a sampling time of 120 s was used throughout all measurement conditions to ensure sufficient number of seeding particles passed through the LDA measurement point.

Due to the limitation of the test rig, it is difficult to maintain a constant base amplitude up to 84 Hz where the second resonance occurs. In addition, cavitation was observed when the beam was forced at 40 Hz with a base displacement of 1.2 mm. This introduces complexities which are out of the scope of this work. Therefore, a maximum forcing frequency of 35 Hz was considered, limiting this study to the first resonance of the beam. The frequencies of 4 Hz, 9 Hz and 14 Hz were chosen in order to investigate the fluid velocity induced by the beam when vibrating in the first mode shape. The frequencies of 18 Hz, 23 Hz and 30 Hz were selected because the beam vibration, at those frequencies, is composed of both the first and the second mode shapes. The location of the selected frequencies with respect to the FRF is shown in the left panel in Fig. 5. The right panel in Fig. 5 displays the normalised LDA fluid velocity profiles with respect to the maximum base velocity of the beam for various frequencies generated with a constant base amplitude of 1.2 mm. It is seen from the figure that the mean fluid velocity at 4 Hz fluctuates around zero. This is due to the very low base input velocity for the beam which was estimated to be approximately 0.03 m/s. The negative mean velocity is discussed in Section 3.2.

At 9 Hz, the maximum fluid velocity is approximately equal to the base input velocity of the beam. At the first resonance, 14 Hz, the input base velocity is about 0.11 m/s which can generate a maximum fluid velocity of 0.15 m/s. At 18 Hz, the input base motion increases to 0.14 m/s with the fluid velocity decreasing to 0.12 m/s. With the base input velocity of 0.17 m/s, the beam at 23 Hz can only induce a maximum fluid velocity of 0.1 m/s. Although a maximum mean fluid velocity of 0.14 m/s can also be achieved at 30 Hz, the base velocity of the beam at this frequency is 0.23 m/s, which is much higher than the 0.14 m/s corresponding to the 18 Hz case. It can be seen from the right panel in Fig. 5 that the peak fluid velocity increases until 14 Hz, then decreases for 18 Hz and 23 Hz, to increase again for the 30 Hz case. This behaviour follows the trend of the FRF magnitude.

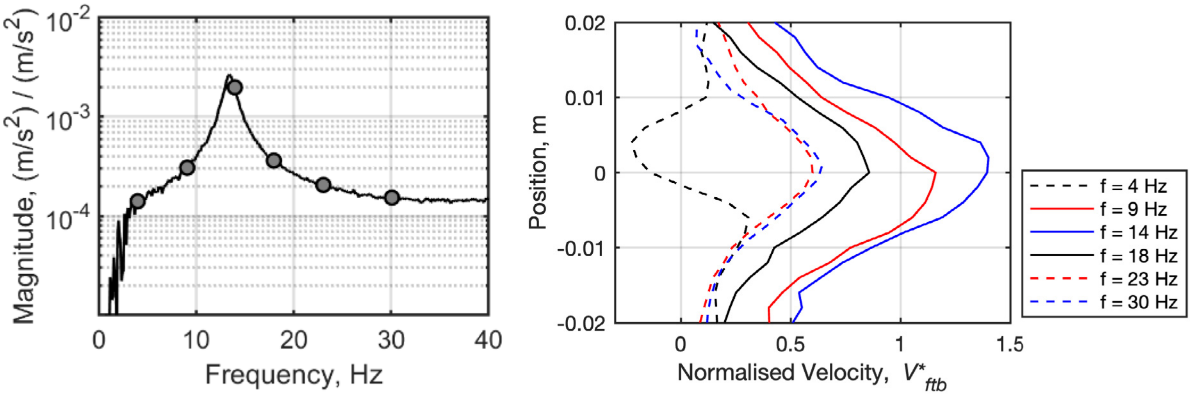

(a) **(b)**

Fig. 5. (a) Location of the forcing frequency in the beam FRF and (b) influence of forcing frequencies on the mean fluid velocities.

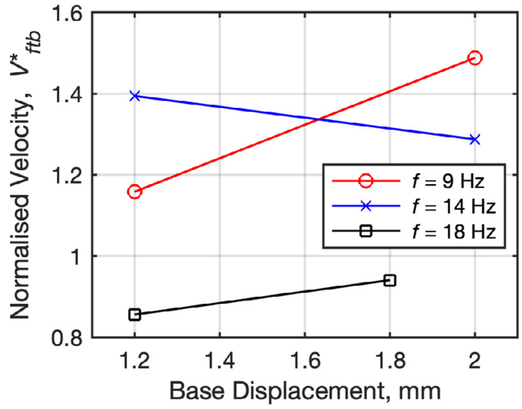

Fig. 6. Influence of the base amplitudes on the normalised velocity.

Fig. 6 shows the influence of the base amplitudes on the fluid velocities at various frequencies. It is seen that in general higher base amplitudes correspond to higher fluid velocities. There is a nonlinear trend between the maximum fluid velocity and base amplitude, demonstrated by the fact that these measurements do not belong to the same plane. At 9 Hz for instance, the maximum fluid velocity is 0.17 m/s generated with the base input displacement and velocity of 1.2 mm and 0.11 m/s, respectively. The normalised velocity, i.e. the ratio of the maximum mean fluid velocity to the base input velocity, generated with the base amplitude of 2 mm is 1.3 higher than that of the base amplitude of 1.2 mm. Although, at 14 Hz i.e., the resonant frequency, increasing the base amplitude from 1.2 mm to 2 mm results in decreasing V^*_{ftb} by about 8%, the maximum mean fluid velocity increases from 0.15 m/s to 0.22 m/s. An insignificant change also occurs at the frequency of 18 Hz, where increasing the base amplitude only affects 10% of V^*_{ftb}. Therefore, there is a nonlinear correlation between the base motion of the beam and the mean fluid velocity. This finding is in agreement with the previous studies reported in Piñeirua et al. (2017) where vibrating at the second mode shape generates less reactive thrust than the first mode shape. They noticed that due to the presence of a node at approximately 0.75L in the second mode shape of the beam, the motion of the beam at the length of about 0.75 L to 1 L (or from the nodal point to the free tip of the beam) contributes to generating reactive thrust, while at 0 L to approximately 0.75 L (or from the base input to the nodal point), it produces resistive or drag force. On the contrary, the beam vibrating in the first mode shape generates reactive thrust almost all along the beam length. Another factor that may contribute to the nonlinear relationship presented in Fig. 6 is the difference in the slope value around the tip of the beam when vibrating at the first and second modes as reported in fishtail studies (Matta et al., 2019; Zurman-Nasution et al., 2021). They showed that in low frequencies the largest sweep angle could lead to lower thrust generation than the lower values.

To further explore the region between the first and second resonant, another beam with a reduced thickness of 0.3 mm was used. The beam length and width are the same as the previous one. The beam density is 8631 kg/m^3. Using the same procedures, Fig. 7 displays the FRF magnitude of the beam with the thickness of 0.3 mm vibrating in air and water. The first-three natural frequencies for the beam vibrating in air are approximately 12 Hz, 75.5 Hz and 214.3 Hz. Using Eq. (1), these frequency values result in a mean modulus of elasticity of 178 GPa. For the measurements in water,

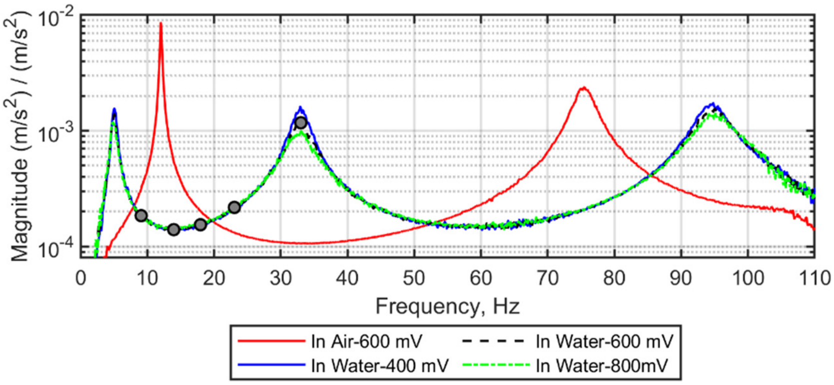

Fig. 7. FRF of the beam with the thickness of 0.3 mm.

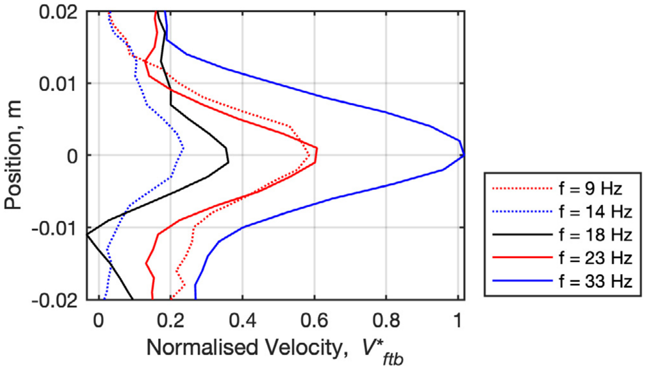

Fig. 8. Velocity profiles of the 0.3 mm beam generated with the constant base amplitude of 1.2 mm.

the first three natural frequencies are approximately 4.98 Hz, 32.9 Hz and 94.8 Hz, which result in the mean flexural rigidity of 0.0046 N m^2. It is noticed that the discrepancy in the estimated mean flexural rigidity for measurements in air and water is increased to 9.6%, compared to the thicker beam model. This may be due to the approximation of the analytical approaches that are based on the theory of a fixed rigid body subjected to an oscillating flow (Morison et al., 1950). Therefore, it provides a good approximation for rigid beams and tends to become less accurate for more flexible beams.

To investigate the region between the first two resonances for the 0.3 mm beam vibrating in water, frequencies of 9 Hz, 14 Hz and 18 Hz were arbitrarily selected so that the influence of the mode shape can be considered in the analysis. A forcing frequency of 33 Hz was considered to examine the fluid dynamics while the beam vibrates at the second resonance. The location of these forcing frequencies in the beam FRF is depicted in Fig. 7 with grey circle markers. Using the same fluid measurement methods, Fig. 8 displays the fluid velocity profiles for various frequencies generated with a constant base amplitude of 1.2 mm. At 9 Hz, the maximum fluid velocity is approximately half of the base input velocity which is estimated at about 0.07 m/s. The deviation between the fluid and base velocity doubles at 14 Hz where the base input velocity of 0.11 m/s can only produce a horizontal fluid velocity of 0.025 m/s. The ratio of the maximum fluid velocity to the base input begins to increase after passing 14 Hz. Eventually, V^*_{ftb} becomes unity at the frequency of 33 Hz or at the second resonant. It is noticed from the figure that the peaks of the fluid velocity profile match the trend of the FRF magnitude. For instance, the lowest FRF magnitude in the first two peaks is observed at 14 Hz which coincides with the lowest fluid velocity among the selected frequencies. It can be concluded that there is a dependency of the fluid velocity on the beam FRF. This phenomenon is further investigated with numerical simulations in the next section.

3. Numerical study and analysis

3.1. Numerical setup

The Computational Fluid Dynamics (CFD) model for simulating a three-dimensional fluid–structure interaction (FSI) consists of three domains: the solid (beam), the overset boundary, and the background fluid (tank) domain. The beam dimension was taken from the experimental measurements provided in Section 2. The total beam length of 0.135 m

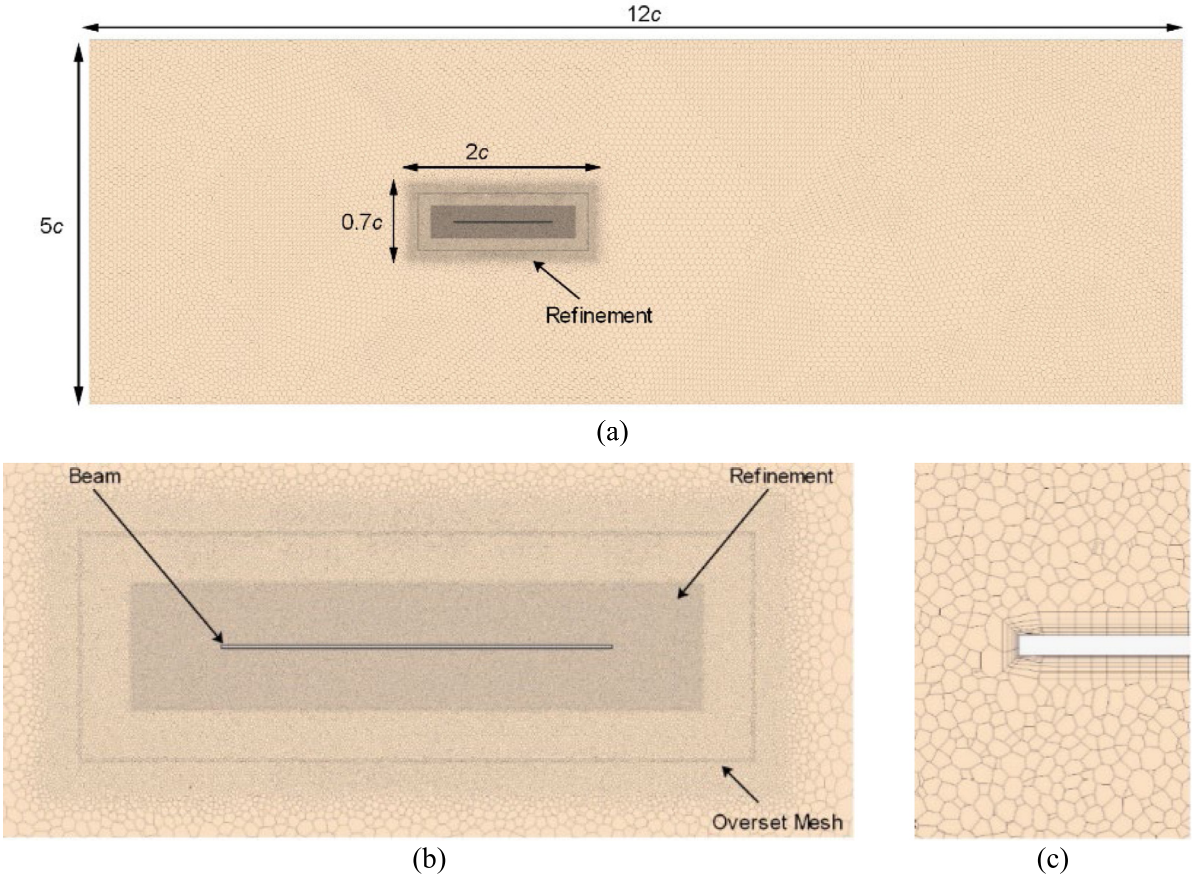

(a)

(b) (c)

Fig. 9. (a) Global mesh domain; (b) Overset and background boundary; and (c) Boundary layer around the beam.

is defined as 1 chord length, denoted as c. Accordingly, the beam thickness of 0.6 mm is equal to 0.0044c. Since the structure is symmetric, a half model was used to reduce the computational time. This results in a beam width of 0.047c. The geometry of the background boundary was 12c x 5c x 0.5c, whilst the overset boundary was 2c x 0.7c x 0.1c as shown in Fig. 9(a). The background boundary was extended to ensure the numerical stabilities were achieved. A three-dimensional mesh was generated with the built-in mesh feature in STAR-CCM+. The solid domain mesh was constructed with a hexahedral mesh. The overset and background boundary mesh were created with an unstructured polygonal mesh and a structured prism layer applied at the solid surface. An illustration of the coordinate axis system, global mesh domain and mesh visualisation are presented in Fig. 9.

A surface control was applied to the background mesh, allowing the structured mesh to grow from the near fields of the overset mesh to the far fields. The far field was set to 20 times of the base size value. A single volumetric control was applied to the background and overset meshes to ensure that the two regions have the same cell size. This is to prevent overlap between the two regions which may alter the flow features. The mesh size of the overset boundary was set to 50% of the base size value. A prism layer was applied to the beam surface of the overset boundary. The total height of the near wall prism layer was set to 0.0056c, specified with 10 number of layers.

The unsteady FSI simulation was performed in STAR-CCM+. For the flow physics and solver, the conservation equations for mass and momentum were solved with the "Segregated Flow" model with the constant density assumption for the equation of state models. The computation used the Reynolds-Averaged Navier–Stokes (RANS) equations with the $k-\omega$ SST Menter model for turbulence modelling methods. The All-Y+ built-in function in STAR-CMM+, capable of dealing with a wide range of near-wall mesh densities, was used for the wall treatment. The density and dynamic viscosity of water were set to 997.561 kg/m^3 and 8.8871E−4 Pa-s, respectively. Accordingly, the Reynolds numbers in this study, estimated using an equation in Sader (1998) and Xiu et al. (2018) with ρ = 997.561 kg/m^3, η = 0.0010016 N s/m^2, b = 0.01275 m and vibration frequency varying from 9 Hz to 33 Hz, are within the range of $2300 \leq \text{Re} \leq 8400$. The boundary conditions for the background domain were set to the following configurations: (1) Wall for the right, left, top, bottom and back surface; and (2) Symmetry plane for the front surface. The "Solid Displacement" module was applied to the solid domain to simulate the transverse vibrations of the beam. The dynamic beam behaviour under loading conditions

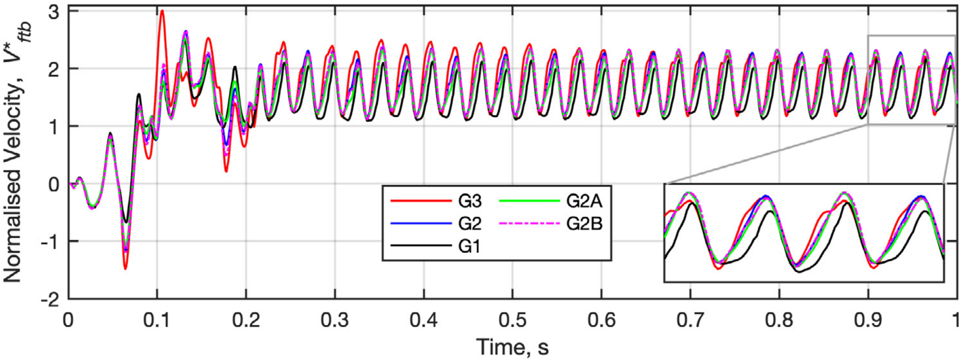

Fig. 10. The time series of fluid velocities at the coordinates of $x = 0.137$ m and $y = 0$ m.

was evaluated with the "Solid Stress" model which is based on the finite element approach. The material was assumed to be isotropic with a linear elastic stress–strain relationship. The boundary conditions of the solid domain were set to the following configurations: (1) Symmetry plane at the front surface, (2) Free at the top, bottom, back and right surface, and (3) Constraint with prescribed displacement at the left surface. The displacement input was of a sinusoidal wave with the amplitude and frequency values taken from the experiment and applied only in the y-direction. A two-way FSI coupling was performed directly within STAR-CCM+ to provide continuous interactions between fluid and solid solvers. The "Mapped Contact Interface" model was used to facilitate the beam and surrounding fluid exchanging displacements and fluid forces at every time step. The "Morphing Motion" module, available in the STAR-CCM+'s built-in features, was applied to the overset region to follow the deformation of the beam. Accordingly, the overset domain provides two region interfaces: the solid–fluid and fluid–fluid interface.

For the unsteady simulation, a temporal 2nd-order discretisation with a temporal resolution of at least 71-time steps per period was used. The simulation was stopped once the beam and fluid responses reached the steady state, which was around 1 *s* to 2 *s* depending on the forcing frequency. The dynamic responses of the beam and the local velocity around the beam tip were saved at each step, paying attention that the residuals (continuity, x-momentum, y-momentum and z-momentum) reached a value below 1.0×10^{-4}.

The CFD model was validated against experiment data: measurements for the beam with the thickness of 0.6 mm and base actuation of 1.8 mm at 18 Hz were used. It is worth mentioning that the validation only considers fluid velocity without including beam responses due to limitations in the test rig. A mesh independence study was performed as part of the validation process: three grids, namely G1 (coarse grid), G2 (medium grid) and G3 (fine grid), were assessed. The total cell count for all domains for grid G1, G2 and G3 are approximately 0.72 million, 2.15 million, and 4.89 million cells, respectively.

Fig. 10 presents the time series of the fluid velocities recorded at the $x = 0.137$ m and $y = 0$ m; for a graphical representation of the measurement location, please refer to Fig. 2. As expected, there is a discrepancy of about 10% based on the mean velocity at the steady state between the base coarse grid, G1, and the most refined grid, G3. Grid G2 achieves a low level of variance compared to grid G3, while achieving an approximate 44% reduction in the total cell count. To investigate the influence of the prism layer height on the time series of the fluid velocities, two grids G2A and G2B with prism layer heights of $0.002c$ and $0.0075c$, respectively, were analysed, where c indicates 1 chord length. It is evident from Fig. 10 that the variation of height considered in G2A and G2B do not affect in a significant manner the fluid velocity. Fig. 11 displays the comparison of the mean fluid velocity between the numerical simulation and experimental data. It is worth mentioning that the mean velocities were taken at $x = 0.140$ m. The mean velocities at $y = 0$ m for the coarse mesh G1 and the finer mesh G2 drop approximately 40% at just 3 mm from $x = 0.137$ m to $x = 0.140$ m. Although the difference of the peak between the experiment data and the coarse grids is small, the mean velocities for the grids, G1 is non-symmetric, and the peaks are offset from the zero point. On the contrary, grid G2 provides a symmetric average velocity, whilst the peak is almost aligned with the experiment data. Therefore, grid G2 is selected to be used in the study. It is observed that discrepancies exist between the experiment and simulation at the measurement location away from the centre, particularly from ±0.005 m to ±0.02 m. Those locations are where the beam tip, vibrating with a peak-to-peak amplitude of approximately 0.004 m, has minimum influence on the induced flow. The water might circulate in the tank with a low velocity and, hence, contribute to overestimating the measured velocity value. However, the flow around the centre of measurement points should not be affected by this occurrence, demonstrated with an identical velocity profile between the experiment and simulation.

3.2. Simulation results and discussion

Numerical simulations using the grid model G2 were used to expand the mean velocity results obtained experimentally using the beam with the thickness 0.6 mm. The base amplitude was set to a constant value of 1.2 mm and the forcing

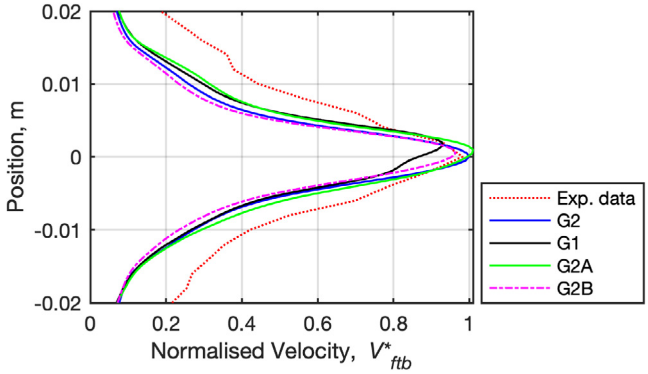

Fig. 11. Comparison of the mean fluid velocity of the experimental data and numerical simulation.

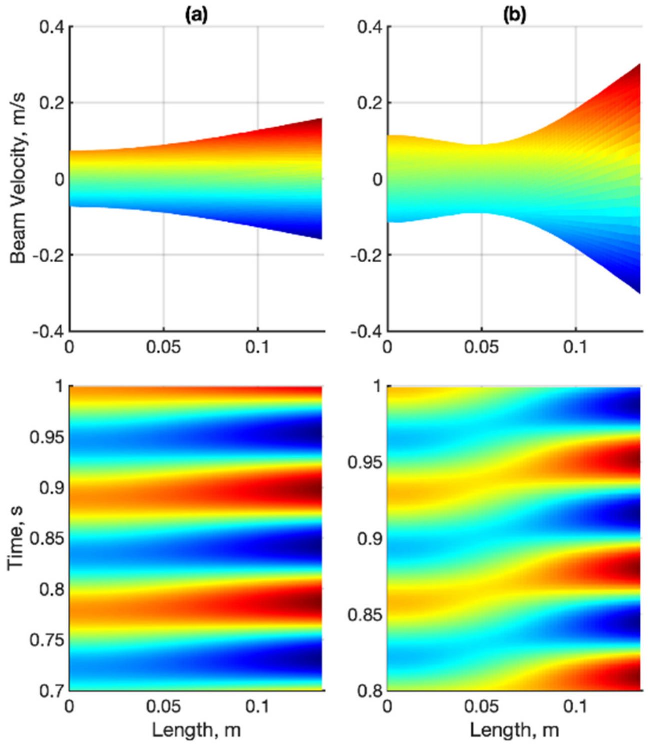

Fig. 12. Velocity responses of the 0.6 mm beam at (a) $f = 9$ Hz and (b) $f = 14$ Hz. The first row represents the beam envelope and the second row represents the propagation wave over time; hence the velocity magnitude of the second row can be read from the first row.

frequencies were varied based on the experimental data. Fig. 12 presents the steady state velocity responses of the 0.6 mm beam for various forcing frequencies. It is worth mentioning that the beam velocity was represented in a 3D plot with respect to the time and beam length. Therefore, the first row of Fig. 12 displays the velocity envelope or the front view of the 3D plot which describes the velocity amplitude over the beam length, while the second row shows the top view of the 3D plot which depicts the propagation of the wave over time. Note that the reader can refer to the beam envelope to read the magnitude of the propagation wave over time. At $f = 9$ Hz, it is observed that the beam vibrates in the first mode shape and the base input and the tip are in phase. Due to the damping from the fluid forces, there is a slight phase delay between the base and the free tip in the vibration pattern. The ratio between the tip and base input velocity is 2.17. At $f = 14$ Hz, the tip velocity ratio increases to 2.66 and the phase delay between the base and the free tip becomes more noticeable. The maximum phase delay is achieved when the forcing frequency equals the natural frequency: from the beam equation, one obtains that the damping contribution is the highest and it is responsible for maximising the amplitude of the travelling waves (Syuhri et al., 2022).

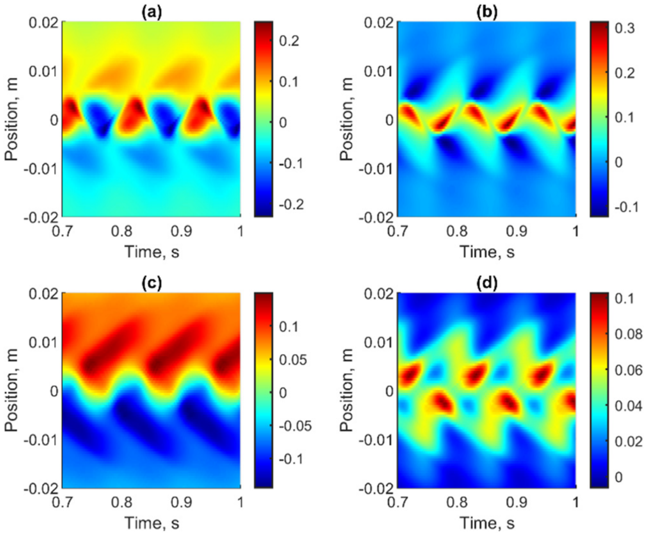

Fig. 13. The time series of fluid velocities of the 0.6 mm beam generated at $f = 9$ Hz probed at (a)–(b) $x = 0.136$ m and (c)–(d) $x = 0.140$ m; where (a) and (c) depict the vertical fluid velocity, whereas (b) and (d) are horizontal fluid velocity. Note that the transient responses from $t = 0$ s to 0.7 s are not included.

To demonstrate the fluid behaviour due to the first mode shape, Fig. 13(a) and (b) show the time history of the fluid velocity in the vertical and horizontal direction, respectively, located at $x = 0.136$ m actuated with the forcing frequency of 9 Hz (note the different scales are used for the panels in Fig. 13 to better highlight the features of the flow). From these figures, it can be seen that the fluid velocity in the vertical and horizontal directions reaches its maximum amplitude at the same time and the same location. By comparing Fig. 12(a) and Fig. 13(a), the fluid velocity is 90 degrees out of phase relative to the beam velocity. For the horizontal fluid velocity component shown in Fig. 13(b), the local maximum values are 0.31 m/s. Due to the fluctuation in the time series, the mean velocity of the horizontal component along the central axis of the undeformed beam ($y=0$) is estimated to be 0.17 m/s, which is about half of the local maximum values. Fig. 13(c) and (d) display the time series of the vertical and horizontal fluid velocity components at $x = 0.140$ m, respectively. It is observed that the fluid velocity drops about 54% compared to the measurement at $x = 0.136$ m. The mean velocity of the horizontal velocity component is 0.076 m/s which is comparable to the result obtained from the experiment shown in Fig. 6. High fluctuations in the fluid velocity were also discovered at $f = 14$ Hz where the maximum horizontal velocity at $x = 0.136$ m is 0.58 m/s, while the maximum mean velocity is only 0.3 m/s (note that the results are not shown here for brevity).

The behaviour in Fig. 12(a) and Fig. 13(b) explains the negative value in the mean velocity of the experimental data at $f = 4$ Hz shown in Fig. 8. At low frequencies, the ratio between the free tip and the base displacement is approximately equal to unity and the beam undergoes a quasi-rigid body movement. Due to pressure differences generated by this quasi-rigid body movement, positive pressure gradients push the fluid in the positive direction, whilst negative pressure gradients draw in fluid from the domain. Consequently, due to the oscillations, the mean velocity becomes small, and in some regions the average value of the horizontal velocities becomes negative. For instance, the mean velocity at $y = 0.005$ m and $x = 0.136$ m shown in Fig. 13(b) is -0.016 m/s. The numerical simulations also confirmed the nonlinear dependency between the mean fluid velocity and the base amplitude noted in Fig. 6. This is mostly due to the quadratic nature of the damping function in the beam equation: increasing the input amplitude increases the velocity of the beam which causes a considerable shift in the damped natural frequency. Consequently, the beam free tip to base displacement ratio, particularly near resonance, changes with the input amplitude.

Fig. 14(a) and (b) depict the beam velocity responses at 23 Hz and 30 Hz, respectively. The tip velocity ratio at $f = 23$ Hz is estimated to be 1.96. After the first resonant frequency, the beam response is comprised of the first two mode shapes (the contribution from other modes is negligible). Note that the free tip and the base of the beam at the second mode are 180 degrees out-of-phase. For pure standing waves, this creates a node in the deflection with consequent zero displacement. In the presence of damping, there is a phase delay which makes the amplitude at the node non-zero as demonstrated by the velocity envelope at $f = 23$ Hz and $f = 30$ Hz in Fig. 14. In addition, the position of the node tends to shift to the free end of the beam. It is also worth noting that when the amplitude of the oscillation reduces, the contribution of the surrounding fluid to the damping force is considerably smaller. Therefore, the phase delay between the displacement at the extrema of the beam also becomes smaller.

At $f = 30$ Hz, the tip velocity ratio is about 1.06. Fig. 15(a) and (b) present the time series of the horizontal fluid velocity located at $x = 0.136$ m and $x = 0.140$ m, respectively (the reader should note the different scales used in Fig. 15

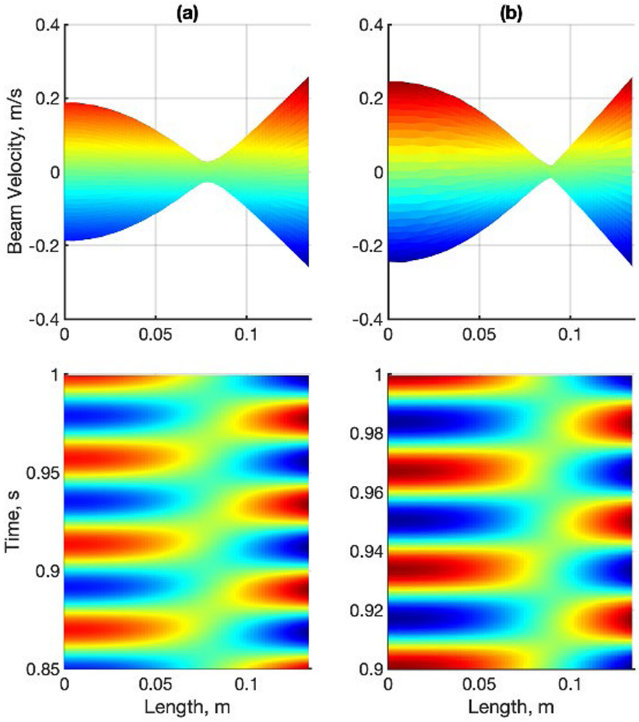

Fig. 14. Velocity responses of the 0.6 mm beam velocity at (a) $f = 23$ Hz and (b) $f = 30$ Hz.

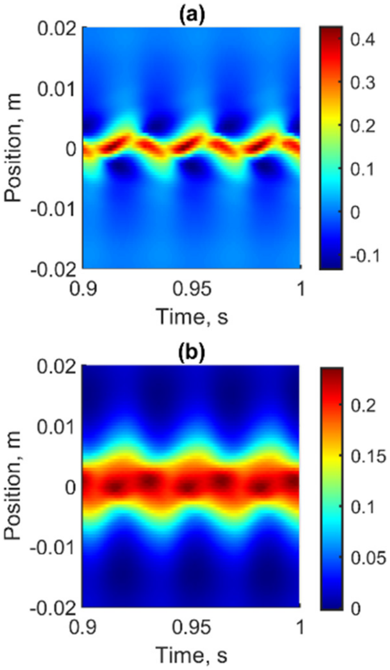

Fig. 15. Time series of the fluid velocity at $f = 30$ Hz probed (a) $x = 0.136$ m and (b) $x = 0.140$ m.

the two pictures, necessary to highlight the characteristics of the induced flow). It is seen from the visual observation that the fluid velocity is more uniform than that of the beam vibrating in the first mode shape. This can be caused by the decrease in the tip velocity ratio.

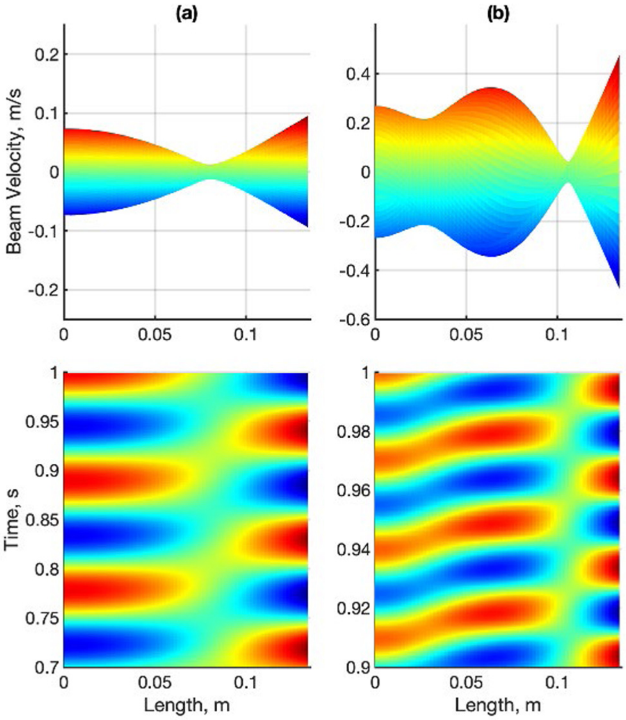

Fig. 16. Velocity responses of the 0.3 mm beam at (a) $f = 9$ Hz and (b) $f = 33$ Hz.

To further investigate the fluid characteristics of the 0.3 mm beam, the thickness of the solid domain of the CFD model was altered to 0.0022c. All simulation parameters follow the grid model G2. Fig. 16 presents the beam velocity envelope and vibration pattern of the beam with the thickness of 0.3 mm for various forcing frequencies. The tip ratio at the forcing frequency of 9 Hz and 18 Hz are 1.3 and 1.08, respectively. At $f = 33$ Hz or the second resonant frequency, the tip ratio increases to 1.78, and the vibration pattern presents a noticeable contribution from the travelling waves, indicated by the phase delay between the displacements at the beam extrema. The horizontal fluid velocity components recorded at $x = 0.136$ m for forcing frequencies of 9 Hz and 33 Hz are shown in Fig. 17. It is noticed that at 9 Hz the 0.6 mm beam oscillates following the first mode shape whereas the vibration of the 0.3 mm beam mostly exhibits the characteristics of the second mode shape. By comparing Fig. 13(b) and Fig. 17(a) it can be seen that the fluid velocity at the same frequency of 9 Hz, exhibits less fluctuations when the beam vibrates at the second mode shape than the first mode shape. At 33 Hz, the maximum fluid velocity shown in Fig. 17(b) is 0.90 m/s while the maximum mean velocity is 0.59 m/s.

4. Model development: Two-point excitation beam model

It has been demonstrated with the 0.3 mm and 0.6 mm beams that the maximum travelling waves are experienced near resonance. Nonetheless a meaningful comparison of the effect of travelling waves on the fluid dynamics of the two beams is difficult due to the profound differences between the behaviour of the beam at this frequency and the consequent travelling wave content in the vibration. To generate travelling waves over a wide range of frequencies, the beam extrema need to be actuated so that a 90-degree phase delay in the displacements is created. Fig. 18(a) illustrates the schematic diagram of the two-point excitation model to generate a pure travelling wave. This configuration is a modified version of the artificial swimmers developed in Ramananarivo et al. (2013). The two magnets located outside of the tank are connected to a rotating shaft. This can be used to either attract or repel the permanent magnets located on the beam, generating periodic forces. The 90 degrees out of phase between the beam tips are achieved by arranging the poles of the permanent magnets as illustrated in Fig. 18(a). Since the beam is mounted to the permanent magnets which are assumed to be solid, this configuration no rotation of the cross section of the beam is possible at the tips. By assuming that the magnets undergo rigid body movement without rotation, the beam can be modelled as a clamped–clamped beam with moving supports illustrated in Fig. 18(b).

The 0.6 mm beam was considered in order to study the influence of the travelling waves in the first mode shape of the beam on the dynamics of the surrounding fluid. For the clamped–clamped beam configuration, the first-four values of β_n/L are 4.7300, 7.8532, 10.9956 and 14.1372. Rearranging Eq. (2) and using the beam parameters described in Section 2, the first three natural frequencies of the 0.6 mm beam vibrating in water are approximately 88.88 Hz, 244.99 Hz, and

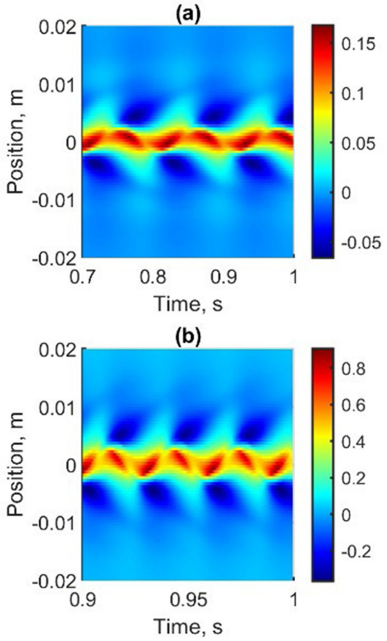

Fig. 17. Time series of the fluid velocity at (a) $f = 9$ Hz and (b) $f = 33$ Hz.

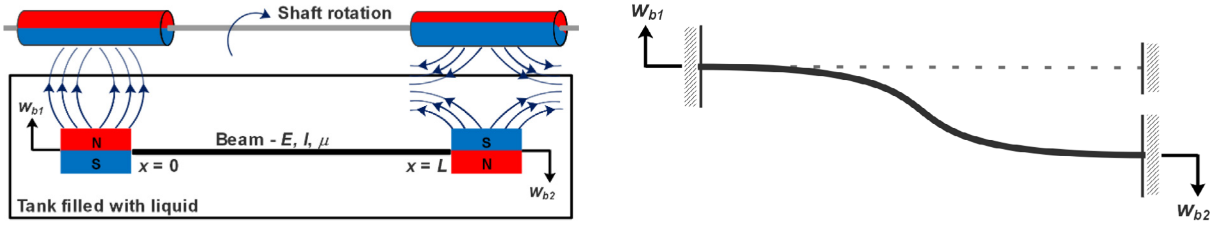

(a) (b)

Fig. 18. (a) Schematic diagram of the two-point excitation beam model, and (b) Schematics of the two-point excitation beam model.

480.29 Hz (Inman, 2013). For the numerical simulations, the two-point excitation model was achieved by assigning the boundary conditions at the left and right walls of the solid domain with a constraint with prescribed displacement. All simulation parameters, including the base input amplitude and forcing frequency, were identical to the 0.6 mm cantilever beam model described in Section 3.1. The base input w_{b1} was set to 90 degrees out of phase relative to w_{b2}. Accordingly, the ratio between the displacement at the tips (tip ratio) of this model would be equal to one for all forcing conditions. Fig. 19(a) and (b) present the velocity envelope and vibration pattern of the two-point excitation model generated at $f = 14$ Hz and $f = 30$ Hz, respectively. At $f = 14$ Hz the vibration for the cantilever and the two-point excitation beam model follows the same pattern even with different beam tip ratios. On the contrary, the two models at $f = 30$ Hz have different vibration patterns due to different mode shapes, even when the ratio between the displacements at the extrema of the beams is the same, i.e., equal to one.

Fig. 20 displays the comparison of the mean horizontal velocity for the cantilever and the two-point excitation beam model presented with the solid and dotted lines, respectively. The cantilever beam provides higher mean velocities than the two-point excitation beam model for the forcing frequencies of 9 Hz to 23 Hz. At the first mode shape, the maximum horizontal fluid velocity is determined by the tip velocity rather than the travelling waves. This can be seen from the mean velocity, particularly at the forcing frequency of 9 Hz and 14 Hz where the two models vibrate in the same mode shape, but in the case of the cantilever beam a mixture of standing and travelling wave is present, whereas in the two-actuation system, the waves are purely travelling. However, when the travelling waves are the sole component in the vibration, fewer fluctuations are observed in the time series of the fluid velocity. For instance, the maximum mean velocity of the two-point excitation model with the forcing frequency of 9 Hz drops from 0.093 m/s at $x = 0.136$ m to 0.065 m/s at $x = 0.140$ m. This is still small compared to the cantilever beam model where the maximum mean velocity decreases by approximately 0.09 m/s just 4 mm downstream. At 18 Hz and 23 Hz, the cantilever beam vibrates at the second mode

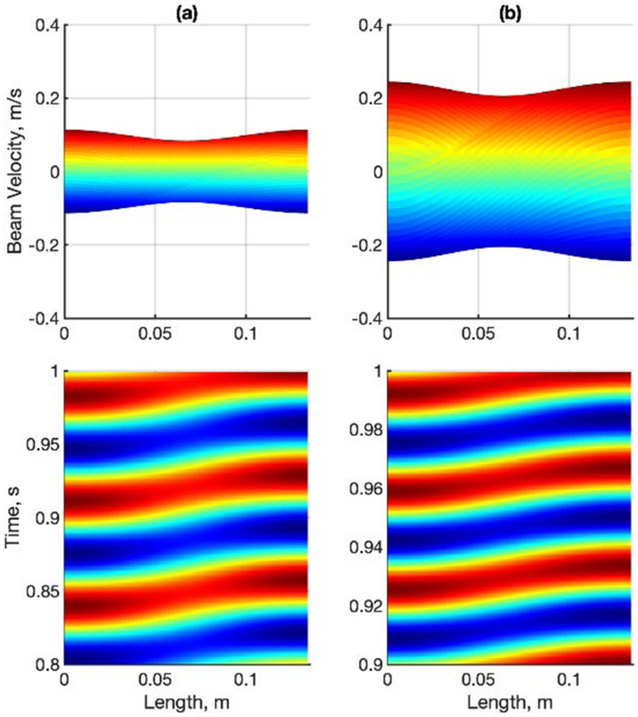

Fig. 19. Velocity responses of the 0.6 mm beam at (a) $f = 14$ Hz and (b) $f = 30$ Hz.

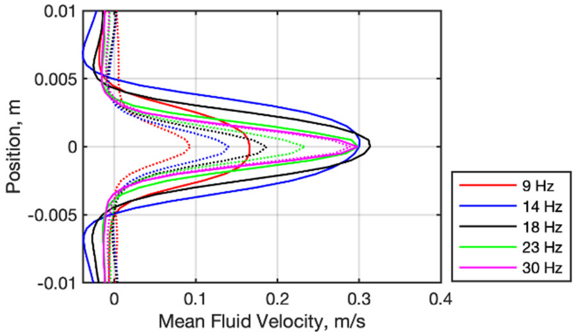

Fig. 20. Comparison of the mean velocity of the 0.6 mm beam for the cantilever (solid-lines) and two-point excitation beam model (dotted-lines).

shape with a 180 degrees phase difference between the two tips, while the two-point excitation model keeps vibrating in the first mode shape. In this case, travelling waves in the two-point excitation model do not significantly increase the mean horizontal velocity. For higher frequencies, namely 30 Hz, the mean velocity of the two models converges. Since the two models have the same tip ratio, this is an indication that at this frequency the vibration pattern (standing vs travelling) does not influence the horizontal fluid velocity.

The 0.3 mm beam is used to compare the two-point excitation and the cantilever models when vibrating in the same mode shape. For the case of the clamped–clamped beam vibrating in water, rearranging Eq. (2) the first three natural frequencies can be obtained: 34.65 Hz, 95.53 Hz and 187.27 Hz. Using the same CFD model for the beam with the thickness of 0.3 mm, Fig. 21 shows the velocity envelope and vibration pattern of the clamped–clamped beam with moving supports for various forcing frequencies. From the figure it can be seen that the node of the second mode shape is gradually formed when increasing the forcing frequency. The inputs for the excitations were set to $w_{b1} = A_f \sin(2\pi ft + \theta_1)$ and $w_{b2} = A_f \sin(2\pi ft + \theta_2)$ where θ_1 and θ_2 were 0 and $\pi/2$ respectively for the first mode: this generates mechanical waves that propagate from 0 m to 0.135 m along the beam. In the second mode shape, there are two antinodes that have a 180 degrees phase shift. Therefore, the phase angle θ_1 and θ_2 at 33 Hz shown in Fig. 21(c) were set to $\pi/2$ and 0, respectively, to maintain the same direction of propagation for the travelling waves.

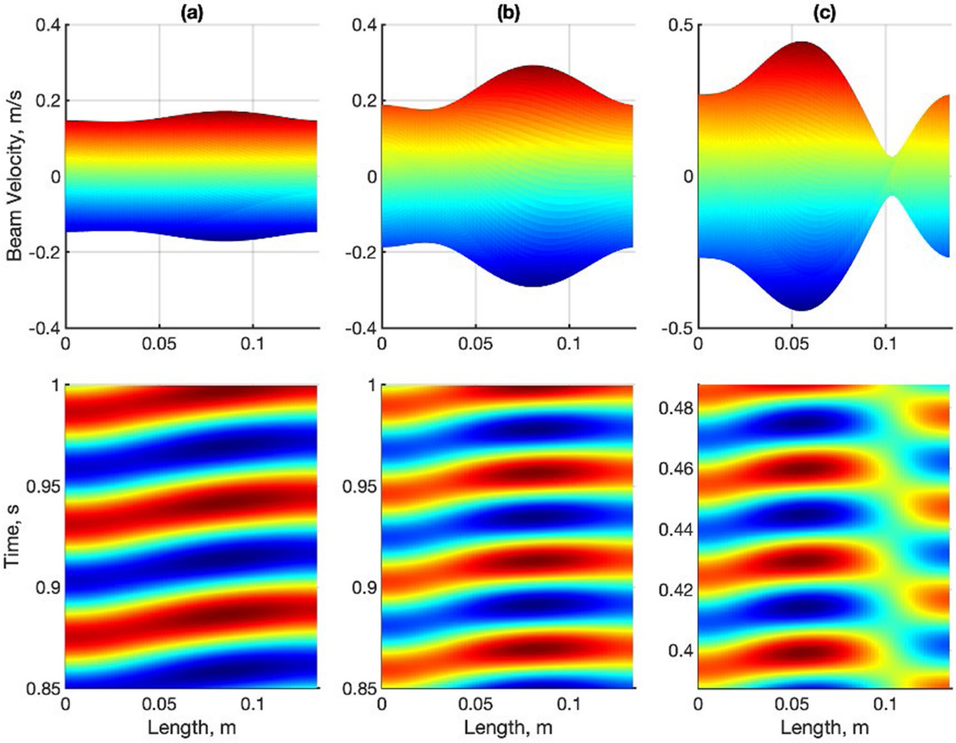

Fig. 21. Velocity responses of the 0.3 mm beam at (a) $f = 18$ Hz, (b) $f = 23$ Hz and (c) $f = 33$ Hz.

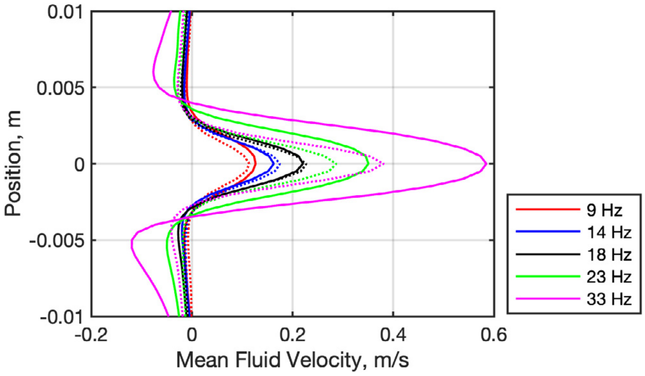

Fig. 22. Comparison of the mean velocity of the 0.3 mm beam at $x = 0.136$ m; the solid and dotted lines represent the cantilever beam and the two-point excitation beam model, respectively.

Fig. 22 presents the comparison of the mean horizontal fluid velocities of the 0.3 mm beam for various forcing frequencies. The cantilever and two-point excitation beam model are indicated with the solid and dotted lines, respectively. The mean velocities of the two models are comparable particularly for the forcing frequency of 9 Hz, 14 Hz and 18 Hz. The same phenomenon can also be seen for the cantilever beam at $f = 23$ Hz, the green solid line, and the two-point excitation beam model at $f = 33$ Hz, the magenta dotted-line, where these two models generate vibration with an identical beam tip velocity value of 0.27 m/s. It can be concluded for the first two resonance that the fluid velocity is dependent of the beam tip velocity. The fluctuation in the time series of fluid velocity is due to the high displacement at the tip rather than the vibration pattern. This can be observed, for instance, at $f = 33$ Hz for the cantilever beam model shown in Fig. 22 where the tip displacement is approximately 2.48 mm. In addition, the vibration pattern, which can be pure travelling, pure standing, or hybrid waves, has minimal effect on the fluid dynamics, particularly for the first two mode shapes.

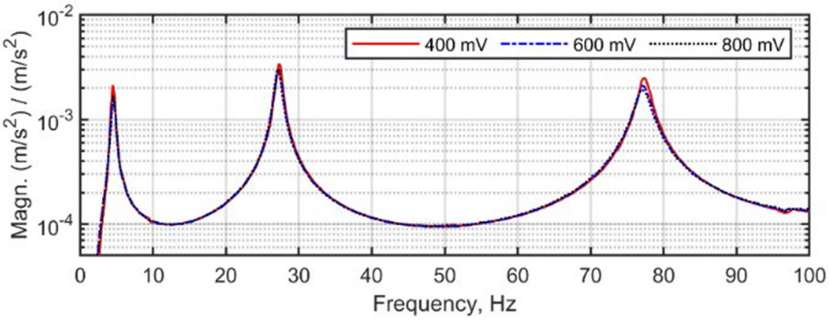

Fig. 23. FRF of the beam with the thickness of 0.1 mm measured in air.

5. Investigation into higher mode

A metal beam with a thickness of 0.1 mm was used to investigate the fluid characteristics up to the fourth beam resonant frequency. The length and width of the beam are the same as the other beams described in Section 2. The beam density is 8500 kg/m^3. Using Eq. (1), the mean flexural rigidity is about 2.231e-4 N m^2. Fig. 23 presents the FRF of the cantilever beam with the thickness of 0.1 mm vibrating in air obtained from experimental measurements with random inputs. The first three natural frequencies are approximately 4.50 Hz, 27.25 Hz and 77.25 Hz. Note that the first torsional natural frequency for a cantilever beam is typically located after the third resonant of the bending (transverse) vibration. The combination of the transverse and torsional vibration can potentially induce other fluid phenomena which are not the interest of this study. Since the experimental equipment is not capable of obtaining the FRF for the torsional vibration, a 3D modal analysis was carried out using ABAQUS. It was found that the first and second torsional resonances are at 89.52 Hz and 268.55 Hz. By assuming that the flexural rigidity of the beam is constant for all media, $EI = EI_w$, Eqs. (1) and (2) can be rearranged to give a relationship between the natural frequencies in vacuum and in water as follows (Koushesh, 2016),

$$f_{n,w} = \frac{1}{\sqrt{1 + \frac{\pi \rho_w b}{4\rho h}}} f_n \tag{3}$$

Substituting the obtained natural frequencies into Eq. (3) results in the undamped natural frequency values of 1.23 Hz, 7.73 Hz, 21.65 Hz, 25.08 Hz and 42.43 Hz. Note that the frequency of 25.08 Hz is the torsional vibration of the beam.

Using the grid model G2 to simulate the dynamic responses of the 0.1 mm beam, the thickness of the solid domain of the CFD model was reduced to 0.00074c. The simulation parameters were identical to the cantilever beam model described in Section 3.1. The ratio of the tip displacement to the base input from the STAR-CCM+ simulation, shown in Fig. 24, is superimposed with the results from the analytical model of a cantilever beam vibrating in water derived in Syuhri et al. (2022). Stepped sine waves were used for the input signal for simulating the analytical model with the forcing frequency varied from 0.5 Hz to 35 Hz and a constant base amplitude of 1.2 mm. It is evident that the analytical model agrees well with the STAR-CCM+ model, except for the forcing frequency of 18 Hz and 23 Hz. These frequencies are around the third resonant of the transverse vibration which is close to the first resonant of the torsional vibration. Since the analytical model only considers the transverse vibration, the discrepancies might be caused by the influence of the torsional vibration on the 3D simulation of the STAR-CCM+ model. Fig. 25 displays the velocity envelope and vibration pattern of the cantilever beam for some of the forcing frequencies. There are 3 nodes in the velocity envelope at $f = 30$ Hz indicating that the beam vibrates in the fourth mode shape. There is also a strong travelling wave pattern at $f = 30$ Hz demonstrated with the phase delay ± 90 degrees between the two tips.

The two-point excitation beam model is used to generate maximum travelling waves for the 0.1 mm beam. The natural frequencies for the clamped–clamped beam configuration vibrating in air are 28.04 Hz, 77.28 Hz and 151.50 Hz. These result in natural frequencies for submerged in water of about 7.85 Hz, 21.65 Hz, 42.43 Hz and 70.15 Hz. Fig. 26 displays the vibration responses of the two-point excitation model generated with the 0.1 mm beam for various forcing frequencies. Note that the phase angle θ_1 and θ_2 of the base inputs for the second mode were set to $\pi/2$ and 0, respectively, to keep the travelling waves in the positive direction. Reducing the thickness of the beam appears to induce more travelling waves for the cantilever beam model which, in turn, leads to wave patterns comparable to the two-point excitation beam model. This phenomenon can be particularly seen, for example, at $f = 30$ Hz where the two models vibrate in different mode shapes with the same tip velocity value. In addition, an identical wave pattern is also observed for the two models at 9 Hz, although the result is not shown here for brevity.

The solid and dotted lines in Fig. 27 present the comparison of the horizontal mean velocities at $x = 0.136$ m for the cantilever and two-point excitation beam model, respectively. The dotted line for $f = 4$ Hz is indistinguishable due to its superimposition with the solid line. The maximum mean velocity is still determined by the tip velocity for the forcing

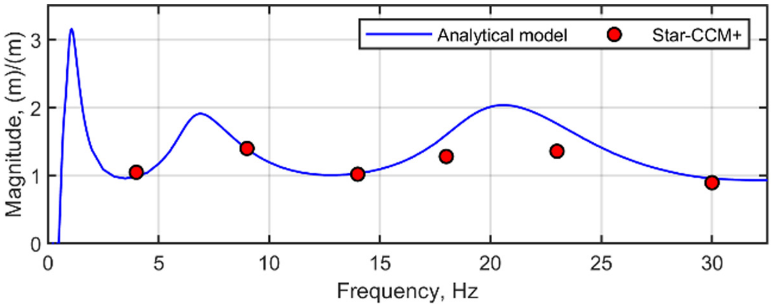

Fig. 24. FRF of the 0.1 mm beam generated with stepped sine waves.

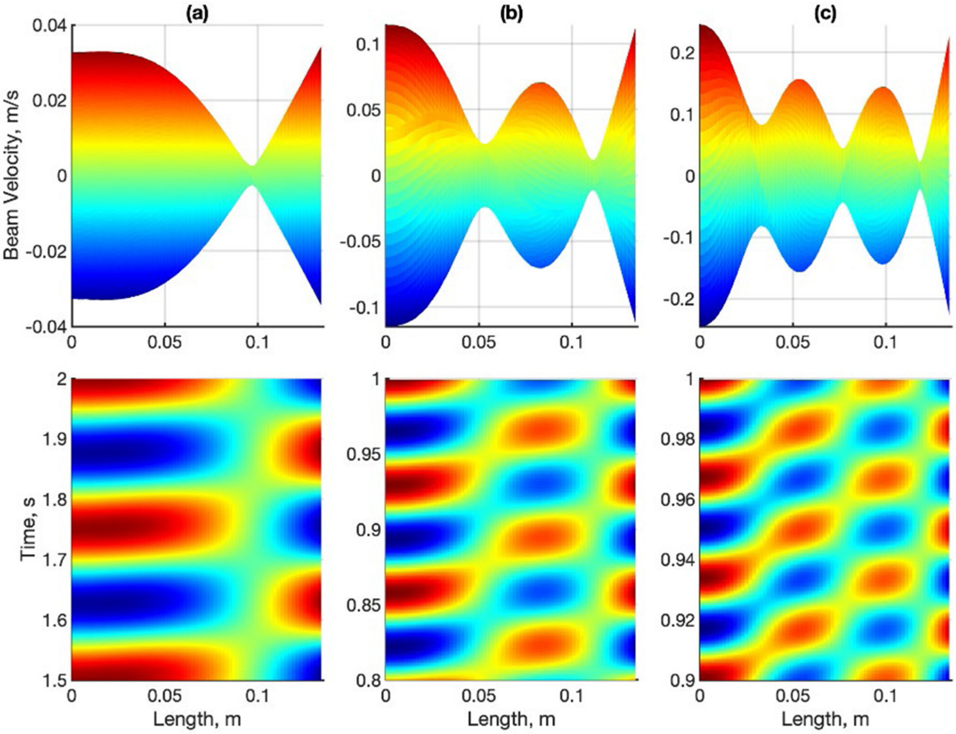

Fig. 25. Velocity responses of the cantilever beam at (a) $f = 4$ Hz, (b) $f = 14$ Hz and (c) $f = 30$ Hz.

frequency up to 9 Hz or the second resonant. The vibration patterns show their influence on the fluid dynamics at 14 Hz. At this frequency, the tip velocity and the tip ratio are equal for both models, while the mean fluid velocity is higher in the two-point excitation model compared to the cantilever beam model. This is an indication that the tip velocity becomes independent of the maximum mean velocity. Following the same trend, the mean velocities superimpose each other at 18 Hz, although the tip velocity of the cantilever beam model is higher than the two-point excitation model. The same incident, where the mean fluid velocity of the two-point excitation model exceeds the cantilever beam, can also be seen at $f = 30$ Hz. Although the two models have a similar tip velocity, about 0.23 m/s with the tip ratio equal to unity, there is a significant difference in the mean fluid velocity. In addition, the fluid velocity at 23 Hz is incomparable since this frequency is located between the third resonant, 21.65 Hz of the bending vibration and the first resonant, 25.08 Hz, of the torsional vibration of the cantilever beam. Therefore, the torsional vibration might also contribute to generate higher fluid velocity responses.

6. Discussion on the variation in the beam thickness and induced fluid velocity

Comparisons of induced fluid velocities for one- (cantilever beam) and two-point excitation beam models have been considered in the previous sections. This section examines the relationship between the induced fluid velocity and

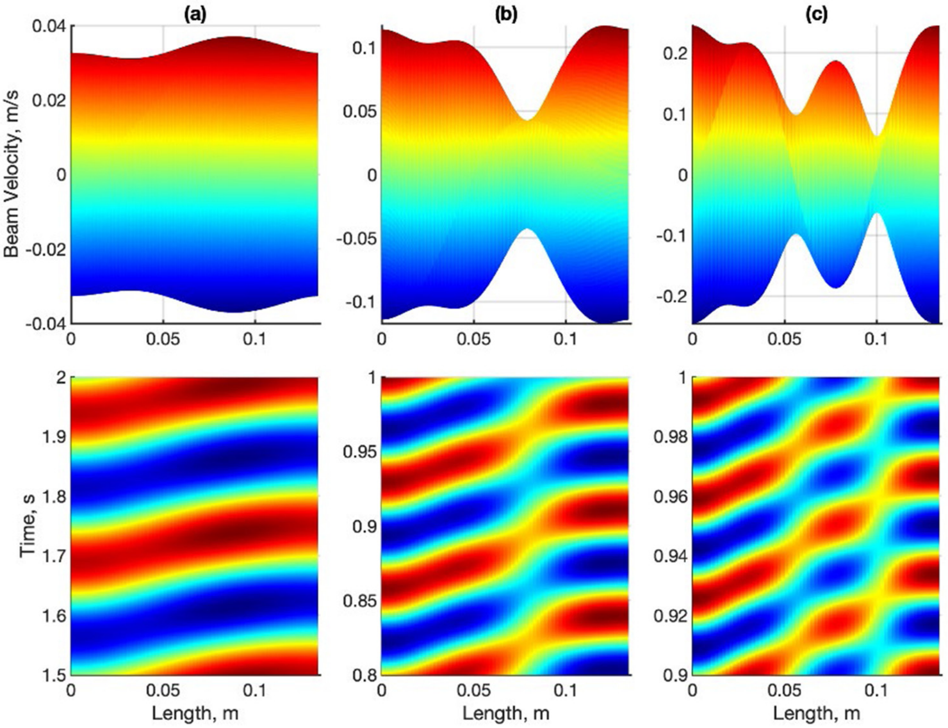

Fig. 26. Velocity responses of the two-point excitation model at (a) $f = 4$ Hz, (b) $f = 14$ Hz and (c) $f = 30$ Hz.

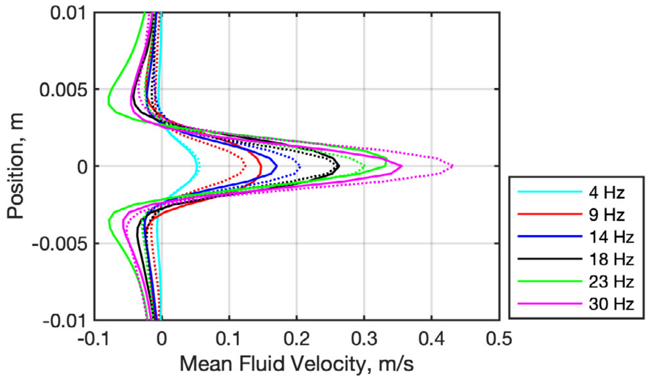

Fig. 27. Comparison of the mean fluid velocity at $x = 0.136$ mm; Solid lines: the cantilever beam model and dotted lines: the two-point excitation beam model.

variation in the beam thicknesses. Fig. 28(a) presents the comparison of maximum beam tip velocity of the two models for various beam thicknesses. It should be noted that the maximum beam tip velocity of the two-excitation beam model for 0.1 mm to 0.6 mm, displayed with the dotted lines, superimposes each other. Fig. 28(b) shows V^*_{ftt}, the maximum mean fluid velocity relative to the maximum beam tip velocity, of the one- and two-point excitation beam models for various beam thicknesses. As anticipated, the trend line of the fluid velocity of the cantilever beam follows the beam tip velocity particularly for frequencies up to 20 Hz. This is where the beams vibrate in the first and second mode shapes; and the induced fluid velocity is mainly driven by the tip velocity. After passing 20 Hz, the 0.1 mm beam generates higher mean fluid velocity with a lower tip velocity compared to the thickest (0.6 mm) beam. This may be associated with the travelling waves in the fourth mode shape that promote a higher fluid velocity for the thinner beam. Moreover, the contribution of travelling waves can also be seen in Fig. 28(b) where the two-excitation models offer superior V^*_{ftt} than the other model for the same beam thickness.

As anticipated, both models agree that decreasing the beam thickness would increase V^*_{ftt}. This is believed to be due to the contribution of the wave speed that propagates from one tip to another tip. This type of wave is also known as the

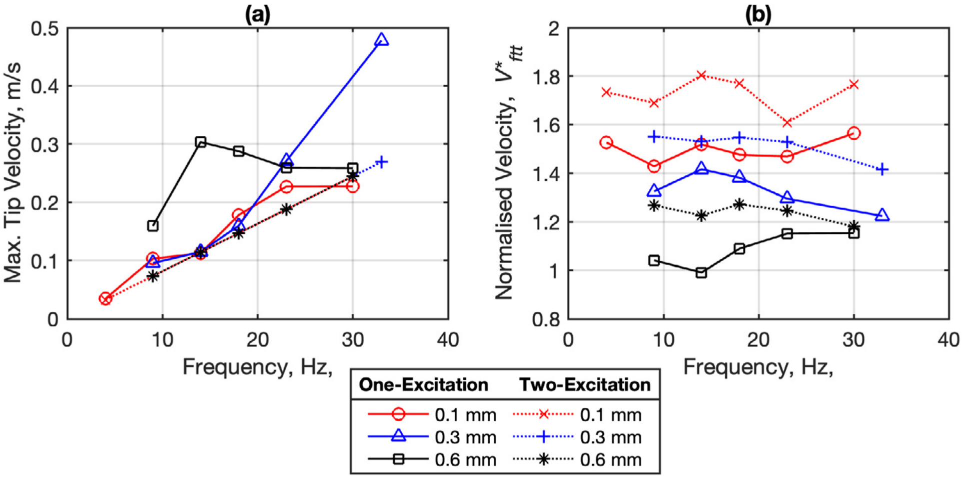

Fig. 28. Comparison of (a) the maximum beam tip velocity and (b) normalised fluid velocity, V^*_{ftt}, for various beam thicknesses using one-point (cantilever beam) and two-point excitation beam models.

propulsive wave speed in swimming animals and is defined as the product of the frequency, f and wavelength, λ (van Weerden et al., 2014). In the beam equation, the latter term is associated with the mode shape of the beam and dictated primarily by the wave number, β_n, given in Eq. (1). For instance, the mode shape of the two-point excitation beam model can be approximated by a sinusoidal waveform with the wavelength function of $n\lambda/2$. Accordingly, reducing the beam thickness would lower the natural frequency which eventually leads to an increase in the wave number followed by the wavelength.

7. Conclusions

This paper investigates the effect of travelling waves on the fluid dynamics of a beam submerged in water. A cantilever beam model subjected to the base motion was considered for the experimental tests to study the characteristics of the mean fluid velocity. In an initial examination, the cantilever beams with thicknesses of 0.3 mm and 0.6 mm operating in the first–second resonant frequencies demonstrate that the normalised fluid velocity with respect to the base input is dependent on the FRF magnitude of the beam. Further examination using numerical simulations reveals that the mean fluid velocity is determined by the tip velocity, while the ratio between the free and base input tips can induce fluctuation in the time series of the horizontal fluid velocity. A two-point excitation beam configuration, capable of generating maximum travelling waves, has been introduced to examine the influence of the travelling waves on fluid dynamics. By comparing the vibration pattern of the cantilever beam and the two-point excitation beam model, it has been shown that the changes in vibration patterns in the first two modes for beams of 0.3 mm and 0.6 mm thickness can promote higher normalised velocity, V^*_{ftt}. Moreover, controlling the tip velocity using the two-point excitation beam model can reduce fluctuations in the time series of the fluid velocity.

To expand the investigation into the higher modes, a more flexible beam with a thickness of 0.1 mm was also examined using the numerical approach developed. This allowed the authors to study the fluid flow induced by the vibrations of the beam up to the fourth resonant frequency. Reducing the beam thickness reduces the natural frequencies as well as the tip displacement and increases the magnitude of travelling waves in the cantilever beam model. For the first two resonant frequencies, this can minimise the velocity fluctuations in the surrounding media; the same effect can be obtained using a two-point excitation approach. Comparing the vibration patterns of the one- and two-point excitation model, it became evident that the mean fluid velocity becomes independent from the tip velocity and relies on travelling waves for higher frequency modes, namely from the third resonance. A proof of this is the fact that the mean fluid velocity of the two-point excitation beam model (pure travelling wave) becomes higher than that of the cantilever beam model (mixture of travelling and standing wave). Furthermore, the comparison between beams of different thicknesses excited in two points revealed that the induced fluid velocity is higher for thinner beams.

In terms of the beam configuration, the cantilever beam model can provide a higher mean fluid velocity, particularly in the case of stiff materials operating at the first two resonant frequencies. However, the tip velocity of the cantilever beam model reduces with increasing frequency and fluid viscosity which makes the ratio between the displacement at the extrema of the beam less than one. Therefore, controlling the free tip velocity might be necessary. Using the two-point excitation beam model, the tip velocity can be kept constant. In addition, travelling waves can be induced over a wide range of frequencies resulting in higher mean fluid velocity, particularly in the case of thin beams operating at higher modes. However, the phase delay between the displacement of the tips needs to be controlled to maintain the waves travelling in the same direction for different mode shapes. The needed phase between the actuations can be found by looking at the phase shift of the antinodes for each mode shape of the clamped–clamped beam configuration.

Our results support the previous observation that the mode shape can affect the induced fluid velocity: the first mode shape induces more velocity than the second mode shape (Piñeirua et al., 2017). Our simulations also support the previous study in Demirer et al. (2022) that the travelling waves can provide efficient locomotion, indicated by higher normalised (fluid-to-beam tip) velocity, V^*_{ftt}. We note that there are nonlinear correlations between the induced fluid velocity and the dynamic behaviour of the beam. Furthermore, these findings would contribute to the development of devices capable of self-propulsion.

Further investigation is required to examine the influence of the torsional vibration in the cantilever beam configuration that occurs close to the third resonant of the bending beam vibration. In the two-point excitation beam model, the effect of rotation induced by the interaction of the permanent magnets with the external magnetic field needs to be considered, since this would induce both rotation and deflection along the beam. In addition, it is also important to investigate the relationship between travelling waves and hydrodynamic thrust, including their swimming efficiency (ratio of mechanical output power to electrical input power to actuate the beam) for various vibration modes and flow regimes.

CRediT authorship contribution statement

Skriptyan N.H. Syuhri: Conceptualization, Formal analysis, Investigation, Methodology, Software, Writing – original draft, Visualization. **David Pickles:** Formal analysis, Investigation, Methodology, Writing – review & editing. **Hossein Zare-Behtash:** Conceptualization, Resources, Writing – review & editing, Supervision. **Andrea Cammarano:** Conceptualization, Resources, Writing – review & editing, Supervision.

Declaration of competing interest

The authors declare that they have no known competing financial interests or personal relationships that could have appeared to influence the work reported in this paper.

Data availability

The authors do not have permission to share data

Acknowledgments

S. Syuhri acknowledged the Islamic Development Bank (IsDB) for providing financial support.

References

Cen, L., Erturk, A., 2013. Bio-inspired aquatic robotics by untethered piezohydroelastic actuation. Bioinspiration Biomim. 8 (1).
Cui, Z., et al., 2018. Complex modal analysis of the movements of swimming fish propelled by body and/or caudal fin. Wave Motion 78, 83–97.
Demirer, E., 2021. Bio-Inspired Locomotion using Oscillating Elastic Plates. Georgia Institute of Technology.
Demirer, E., et al., 2022. Hydrodynamic performance of oscillating elastic propulsors with tapered thickness. J. Fluid Mech. 944.
Dryden, A., Ballard, M., 2021. Numerical investigation of a biomimetic elastic valve for microfluidic pumping. J. Fluids Struct. 103.
Erturk, A., Delporte, G., 2011. Underwater thrust and power generation using flexible piezoelectric composites: an experimental investigation toward self-powered swimmer-sensor platforms. Smart Mater. Struct. 20 (12).
Fernández-Prats, R., et al., 2015. Large-amplitude undulatory swimming near a wall. Bioinspiration Biomim. 10 (1).
Godoy-Diana, R., Thiria, B., 2018. On the diverse roles of fluid dynamic drag in animal swimming and flying. J. R. Soc. Interface 15 (139).
Inman, D.J., 2013. Engineering Vibrations, fourth ed. Pearson.
Koushesh, A., 2016. Added Mass Formulation for Fluid-Structure Interaction. United Arab Emirates, American University of Sarjah.
Liu, G., Zhang, W., 2017. Travelling-wave micropumps. In: Microbial Toxins. pp. 1–19.
Malladi, V.V.N.S., 2016. Continual Traveling Waves in Finite Structures: Theory, Simulations, and Experiments. Virginia Polytechnic Institute and State University, Blacksburg, Virginia.
Malladi, V.V.N.S., et al., 2017. Investigation of propulsive characteristics due to traveling waves in continuous finite media. In: Bioinspiration, Biomimetics, and Bioreplication 2017.
Matta, A., et al., 2019. Effects of fish caudal fin sweep angle and kinematics on thrust production during low-speed thunniform swimming. Biol. Open 8 (7).
Morison, J.R., Johnson, J.W., Schaaf, S.A., 1950. The force exerted by surface waves on piles. J. Pet. Technol. 2 (05), 149–154.
Musgrave, P.F., 2021. Electro-hydro-elastic modeling of structure-Borne traveling waves and their application to aquatic swimming motions. J. Fluids Struct. 102.
Nisar, A., et al., 2008. MEMS-based micropumps in drug delivery and biomedical applications. Sensors Actuators B 130 (2), 917–942.
Ogawa, J., et al., 2009. Development of liquid pumping devices using vibrating microchannel walls. Sensors Actuators A 152 (2), 211–218.
Piñeirua, M., Godoy-Diana, R., Thiria, B., 2015. Resistive thrust production can be as crucial as added mass mechanisms for inertial undulatory swimmers. Phys. Rev. E 92 (2).
Piñeirua, M., Thiria, B., Godoy-Diana, R., 2017. Modelling of an actuated elastic swimmer. J. Fluid Mech. 829, 731–750.
Ramananarivo, S., Godoy-Diana, R., Thiria, B., 2013. Passive elastic mechanism to mimic fish-muscle action in anguilliform swimming. J. R. Soc. Interface 10 (88).

Ramananarivo, S., Godoy-Diana, R., Thiria, B., 2014a. Propagating waves in bounded elastic media: Transition from standing waves to anguilliform kinematics. Europhys. Lett. 105 (5).

Ramananarivo, S., Thiria, B., Godoy-Diana, R., 2014b. Elastic swimmer on a free surface. Phys. Fluids 26 (9).

Raspa, V., et al., 2014. Vortex-induced drag and the role of aspect ratio in undulatory swimmers. Phys. Fluids 26 (4).

Sader, J.E., 1998. Frequency response of cantilever beams immersed in viscous fluids with applications to the atomic force microscope. J. Appl. Phys. 84 (1), 64–76.

Shahab, S., Erturk, A., Underwater dynamic actuation of macro-fiber composite flaps with different aspect ratios: Electrohydroelastic modeling, testing, and characterization. In: Mechanics and Behavior of Active Materials; Integrated System Design and Implementation; Bioinspired Smart Materials and Systems; Energy Harvesting. vol. 2, 2014.

Shahab, S., Erturk, A., 2015. Experimentally validated nonlinear electrohydroelastic Euler–Bernoulli-Morison model for macro-fiber composites with different aspect ratios. In: 27th Conference on Mechanical Vibration and Noise. vol. 8.

Shahab, S., Erturk, A., 2016. Coupling of experimentally validated electroelastic dynamics and mixing rules formulation for macro-fiber composite piezoelectric structures. J. Intell. Mater. Syst. Struct. 28 (12), 1575–1588.

Shahab, S., Tan, D., Erturk, A., 2015. Hydrodynamic thrust generation and power consumption investigations for piezoelectric fins with different aspect ratios. Eur. Phys. J. Spec. Top. 224 (17–18), 3419–3434.

Shelton, R.M., Thornycroft, P., Lauder, G.V., 2014. Undulatory locomotion of flexible foils as biomimetic models for understanding fish propulsion. J. Exp. Biol..

Syuhri, S.N.H., McCartney, A., Cammarano, A., 2020a. Development of an experimental rig for emulating undulatory locomotion. In: IMAC XXXVIII. SEM, Houston, Texas.

Syuhri, S.N.H., Zare-Behtash, H., Cammarano, A., 2020b. Investigating the influence of fluid-structure interactions on nonlinear system identification. Vibration 3 (4), 521–544.

Syuhri, S.N.H., Zare-Behtash, H., Cammarano, A., 2022. Travelling waves of a cantilever beam submerged underwater. [Manuscript in preparation]. University of Glasgow: James Watt School of Engineering.

Wagg, D., Neild, S., 2015. Nonlinear vibration with control. Solid Mech. Appl..

Wang, Y.-N., Fu, L.-M., 2018. Micropumps and biomedical applications – A review. Microelectron. Eng. 195, 121–138.

van Weerden, J.F., Reid, D.A.P., Hemelrijk, C.K., 2014. A meta-analysis of steady undulatory swimming. Fish and Fisheries 15 (3), 397–409.

Xiu, H., Davis, R.B., Romeo, R.C., 2018. Edge clearance effects on the added mass and damping of beams submerged in viscous fluids. J. Fluids Struct. 83, 194–217.

Ye, W., et al., 2014. Travelling wave magnetic valveless micropump driven by rotating integrated magnetic arrays. Micro & Nano Lett. 9 (4), 232–234.

Yeh, P.D., 2016. Fast and Efficient Locomotion using Oscillating Flexible Plates. Georgia Institute of Technology.

Yu, H., et al., 2015. Design, fabrication, and characterization of a valveless magnetic travelling-wave micropum. J. Micromech. Microeng. 25 (6).

Zhang, Z., 2010. LDA Application Methods: Laser Doppler Anemometry for Fluid Dynamics. Springer Berlin, Heidelberg.

Zurman-Nasution, A.N., Ganapathisubramani, B., Weymouth, G.D., 2021. Fin sweep angle does not determine flapping propulsive performance. J. R. Soc. Interface 18 (178).